Pressure Drop in High-Density Porous Metals via Tomography Datasets

A. J. Otaru[1] · M. S. Muhammad[1] · M. B. Samuel[1] · A. G. Olugbenga[1] · M. E. Gana[1] · M. R. Corfield[2]

Abstract

This study combines three-dimensional advanced imaging techniques and computational fluid dynamic modelling and simulation (CFD) to characterise the pressure drop of flowing fluid across high-density porous metals utilising high-resolution X-ray computed tomography data. The modelling approach quantifies the combined effects of pore volume fraction, pore connectivity, pore size and morphology on the flow behaviour of porous metals and to study in more detail the pressure drop behaviour characterised by the sudden change in pore volume by stacking of differential porous samples at the pore-level. The resulting predicted values of the pressure drop as a function of superficial fluid velocity ranging from Darcy to turbulent fluid flow regimes were used to account for the permeability (k_0) and Form drag coefficient (C) of these materials. Supportable agreement between CFD modelled data against empirical measurements available in the literature was substantiated. Therefore it is considered that this approach could lead practically to minimizing the number of design iterations required for the processing of novel-attributing porous metallic materials for applications involving fluid flow.

Keywords Porous metals · Pressure drop · Modelling and simulation

The flow of fluids across porous media, typically those made of metals and metal alloys is gaining a wider audience in many fields of science, engineering, environmental and industrial applications due to their ultra-defining characteristics of a high surface area and effective thermal conductivity [1]. A typical example of this is the use of porous metals as a catalyst support system for converting toxic gasses and pollutants in exhaust gases from an internal combustion engine caused by the sintering of hydrocarbons. As load-bearing and vibrational control devices (noise pollution), metal foams could possibly replace synthetic fibres whose production often results in the release of noxious gasses such as NOx and SOx (air pollutants). Other beneficial applications of these materials include thermal exchange in heat exchangers, biomedical devices, energy (oil and gas), aero-engine fluid systems, filters for high-temperature gas and fluid filtration (waste management).

Fluid flow applications in porous metals is in many ways different from fluid flow in soils or granular packed beds [2, 3] owing to the unique combination of high pore volume and surface area associated with porous metals. These attributes enable their suitability as structures that interact with fluids [4–6]. However, there is an applicable theory between packed beds and porous metallic structures [7–13]. For very slow fluid velocity, typified by pore diameter Reynolds number (R_{ED}) below unity, the well-established Darcy's law relates the fluid velocity and unit pressure drop developed across porous structures (Eq. 1). For high-velocity flow of fluid, the Darcy-Dupuit-Forchheimer (Eq. 2) model relates the defined pressure drop per unit flow thickness (∇p) developed across porous materials as a function of the two most important parameters used to describe flow behaviour at very low (permeability, k_o) and high (Form drag coefficient, C) superficial fluid velocities (v_s), fluid dynamic viscosity (η). and fluid density (ρ.).

$$\nabla p = \frac{\eta}{k_o} v_s \tag{1}$$

$$-\frac{\partial p}{\partial x_i} = \nabla p = \frac{\eta}{k_o} v_s + \rho C v_s^2 \quad \text{and} \quad C = \frac{C_F}{\sqrt{k_o}} \tag{2}$$

✉ A. J. Otaru
  otaru_12257@yahoo.com

1 Department of Chemical Engineering, Federal University of Technology, P.M.B. 065, Gidan-Kwanu Campus, Bida Road, Minna, Niger State, Nigeria

2 Department of Electrical & Electronic Engineering, The University of Nottingham, Nottingham NG7 2RD, United Kingdom

Experimental measurements of pressure drop developed across porous metallic structure in [1, 7, 9, 11–13] used the above expressions to account for the permeability (viscous term) and Form drag coefficient (inertial term) of flowing fluid across porous metals varying in degree of pore size, interstices, and porosities (pore volume fraction). Accounting for these terms through experimentation had been proven previously [9, 11–13] and are useful in understanding and quantifying the effects of pore-sucture related parameters and morphological variations on the fluid flow behaviour characterised by porous metals leading to the design of self-supporting porous metallic materials. Operational costs and complexities in the setting up of equipment associated with measurement of the pressure drop developed across these materials can be reduced through accurate modelling of the fluid flow behaviour of these structures. In addition, this model may also be applicable to capture in detail the pore-structure related parameters of these materials (which can be difficult to acquire experimentally) irrespective of their pore morphology and arrangements. This paper, therefore, aims to accurately represent the pressure gradient/pressure drop developed for a moving fluid across commercially available high-density porous metallic structures (Porvair™, Inconel™ and Recemat™) utilising X-ray computed tomography data. This would help in providing insights into the flow information of single (or) stacked samples, and flow entrance and exit effects at the pore-level using 3D advanced imaging tools and computational fluid dynamics (CFD) modelling and simulation.

The research methods used in this study involved the acquisition of high-density porous metals, 3D image reconstruction and processing, meshing and computationally resolving fluid equations. A Zeiss Xradia Versa XRM-500 3D X-ray CT system was used to acquire tomography datasets of Porvair 7PPI, Inconel 450 μm, Inconel 1200 μm, Recemat RCM-NCX 1723 and Recemat RCM-NCX 1116 porous metallic structures with voxel dimensions ranging from 12 to 26 μm. The ScanIP module within Synopsys-Simpleware™, a 3D advanced image processing tool and model generation software package, was used to create a 3D volume and 3D representative volume element (RVE) whose pore volume fraction differed by $\pm 2\%$ from the original samples. The RVE pore volume fraction of individual sample was measured in the ScanIP by taking a Bolean inversion of the processed RVE structure (i.e. converting the structure phase to fluid phase) before measuring the volume fraction of the 3D RVE model. With knowledge of the materials density, a measure of the samples weight were done with a weighing scale to achieve the materials volume and norminal porosity of the "real" samples. A measure of the accurate representation of the processed 3D RVE was achieved through global thresholding and segmentation of the high-intensity grey scale values (high-density light areas)

in the images whilst pore size was measured through use of the watershed segmentation algorithm of the 3D fluid volume. In addition, pore connectivity ("windows") and ligament thickness and sample surface area were measured using in-built statistical tools within the ScanIP. Figure 1 presents a sequential flow chart showing the 3D advanced imaging of the raw sample to 3D reconstructed RVE. Aside from the processed tomography data, 3D model printout of the skeletal phases of the porous materials were also used (scaled, 1:10) to confirm the reliability of the measured pore-structure related parameters obtained from ScanIP with visible pore network and ligament topologies.

Accurate detailed information of the velocity and pressure gradients developed across the porous structures were achieved through meshing and mesh dependence study to quantify any likely trade-off between mesh count (mesh density) and computed values. Optimum mesh density ranging between 2.5 and 3.5 MCells were utilized for a growth rate of 1.3, minimum edge length of $2.7 \times$ voxel dimension and maximum edge length of $6.5 \times$ the minimum edge length for all the samples. Computational fluid dynamics (CFD) modelling and simulation of airflow across these porous materials were performed by resolving fluid equations and selecting the velocity inlet, atmospheric pressure outlet, symmetrical faces and skeletal walls boundary conditions for this process. The Stokes or Creeping flow model was solved for very slow fluid velocity typified by pore-diameter Reynolds (R_{ED}) number below 1. In addition, the Navier–Stokes equation was solved for $1 < R_{ED} < 300$ while the Spalart–Allmaras Reynold Average Navier–Stokes model with undamped turbulent kinetic viscosity 3x its kinetic viscosity was solved within the fluid package of COMSOL Multiphysics™ 5.2 for the single-phase steady state flow characterised by R_{ED} beyond 300 (Turbulence). It is noteworthy to mention that the specification of these fluid flow regimes that led to the choice of an appropriate fluid equation was aided using Reynolds number specified in [14]; suitable for delineating the regimes of manifestation of flowing fluid in porous structures.

Figure 2 presents the 2D (left) and 3D (right) of the velocity (top) and pressure (bottom) streamline and arrow plots for the Porvair 7PPI foam structure indicating the flow of fluid from entrance to exit. The tendency of abridgement and the expansive morphological nature of the porous structures on the flowing fluid is indicated by the colour map in the legends. Evidently, the pore velocity (v_p) of the fluid at the "windows" of the porous matrices is somewhat higher than that at the fluid dominated pores and this often results, as seen, in a build-up of a high-pressure drop in these zones. Also, measurement of the average linear velocity or seepage velocity within the pore space (pore fluid velocity) was observably higher than the superficial fluid inlet velocity (v_s) thereby confirming the reliability and validation of Darcy's
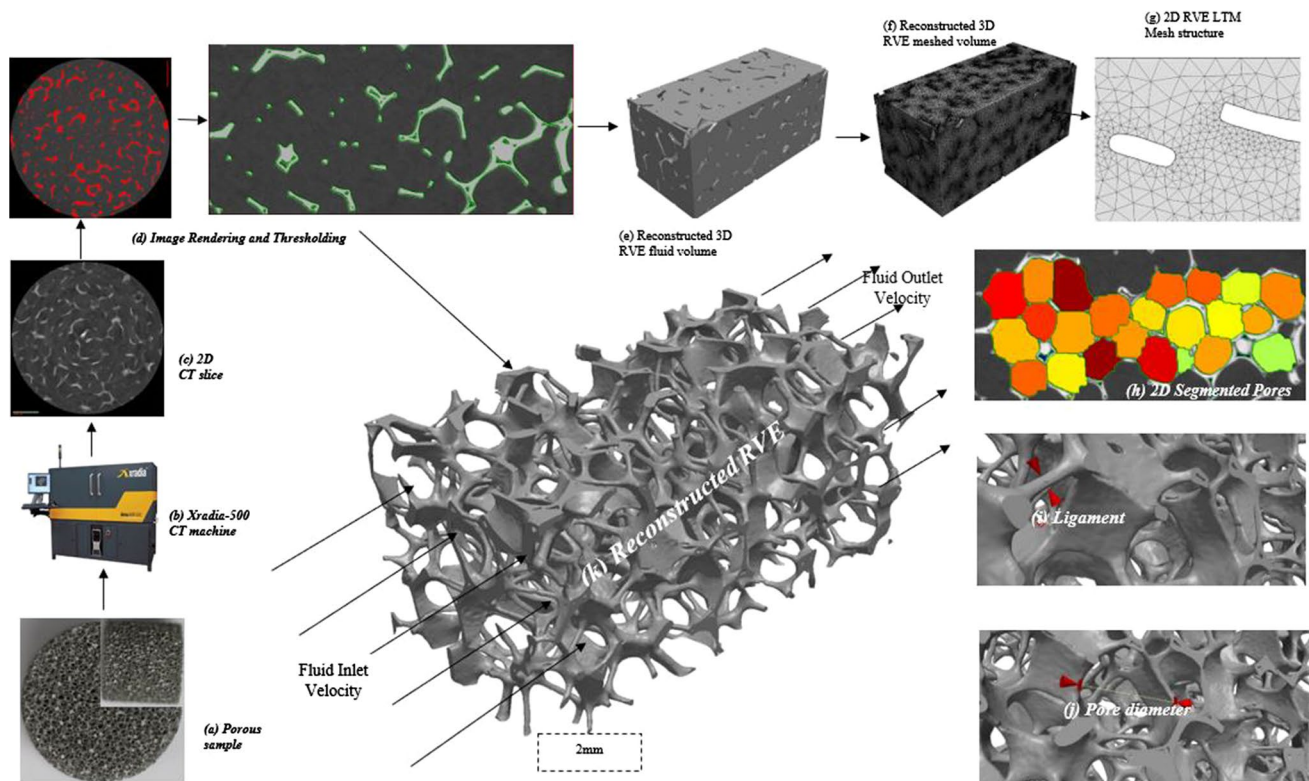
Fig. 1 Representation of the image reconstruction via computed tomography. **a** Porous sample, **b** an Zeiss Xradia Versa XRM-500 3D X-ray CT microscope instrument, **c** high-resolution 2D computed tomography slice data, **d** image rendering and thresholding **e** 3D reconstructed representative volume element (RVE fluid), **f** 3D reconstructed RVE meshed volume, **g** 2D LTM mesh structure, **h** 2D segmented pores **i** 3D RVE Ligaments, **j** 3D RVE pore diameter and **k** 3D reconstructed RVE skeletal phase of Porvair 7PPI porous structure

expression in [15]. This expression is valid for the continuity of fluid flow in porous structures and relates the ratio of fluid superficial velocity to pore volume fraction as the seepage velocity of the flowing fluid.

Figure 3 presents the unit pressure drop developed across the test porous samples as a function of superficial fluid velocity (0–6 m s^{-1}). A tabular presentation of the pore-structure related parameters and flow information extracted by fitting the pressure–velocity data obtained for these samples into Eq. 1 and 2 are presented in Table 1. Figure 3b shows that for a very slow fluid typified by R_{ED} below unity, the relationship between the fluid velocity and pressure gradient/drop is linear (confirming the imposition of the local geometry to dictate the flow field at this purely viscous Darcy regime [16]) and the non-linearity deviation between the fluid flow rate and the driving pressure gradient (Fig. 3a) was observed for high fluid velocity. The computed unit pressure drop developed is highest for the Inc 450 μm and lowest for the RCM-NCX 1116 sample. Interestingly, these are the samples characterised by having the lowest (Inc 450 μm) and highest (RCM-NCX 1116) mean pore sizes (*Dp*) and mean pore connectivity (*Dw*). Moreso, the low-pressure drop obtained for the

RCM-NCX 1116 sample may likely be attributed to its high pore fluid volume (porosity) thereby allowing flowing fluid to fully penetrate its skeletal structures. The extent of the contributing effects of the pore connectivity and pore volume fraction of these materials were further substantiated in Fig. 3b, c using the flow information of the Inc 1200 μm and RCM-NCX 1723 samples where the difference between pore-structure related parameters and flow information is at minimum. Figure 3b shows that the linear pressure gradient achieved for the Inc 1200 μm is higher than that of the RCM-NCX 1723 and this can, therefore, be attributed to the reduced pore connectivity of the Inc 1200 μm sample, hence, reduced permeability compared to the RCM-NCX 1723 sample at this low fluid velocity. As the flow velocity rises beyond Darcy, the pore volume fraction (largely dictated by ligament thickness) of the porous materials becomes significant in defining the gradient of pressure across the porous medium as presented in Fig. 3c. Despite the high-pressure drop obtained for the Inc 1200 μm at slow fluid velocity, the pressure drop for this sample drops below that of RCM-NCX 1116 sample at high-fluid velocity (somewhat beyond 0.4 m s^{-1}), highlighting the contributing effect of low-pore volume
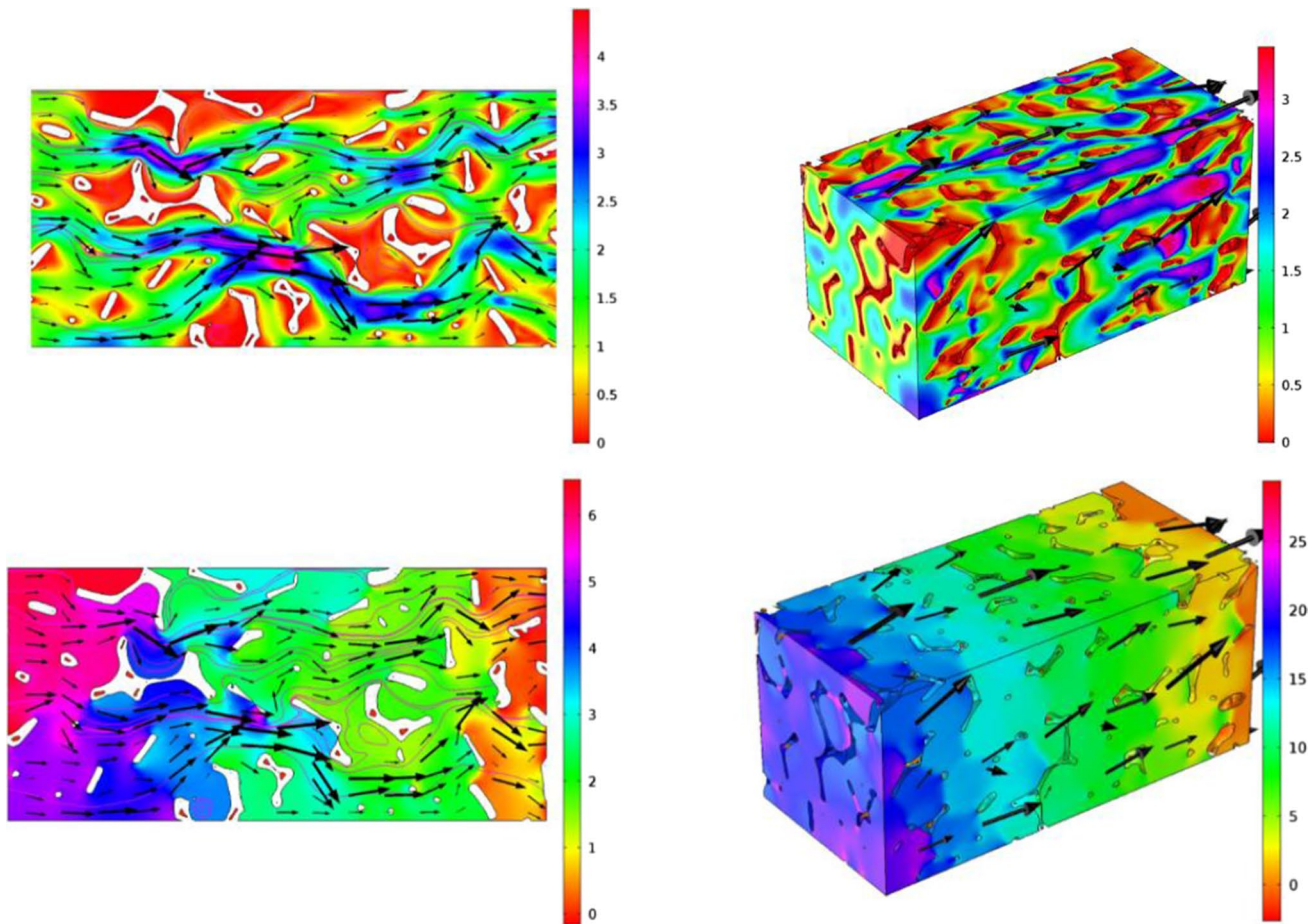
Fig. 2 2D (left) and 3D velocity (top) and pressure (bottom) streamline plots of fluid flow across Porvair 7PPI Foam sample at Laminar superficial fluid flow velocity of 1.0 m s^{-1} (R$_{ED}$=97)

fraction (high surface area) in increasing the drag force between the moving fluid and the pore walls.

An in-depth understanding of the effect of a sudden change in pore volume on the pressure drop of flowing fluid across these samples was made possible by stacking together samples with the lowest (Inc 450 µm) and highest (Inc 1200 µm) porosities as shown in Table 1. This enables an appreciation of the changes associated with a varying pore fluid volume for moving fluid in porous metals. Figure 4(X1) and Fig. 4(X2) present processed images of the 3D volume and 3D representative of the stacked samples while Fig. 4 (Y1, Y2, Z1 and Z2) present the streamline and arrow pressure plots indicating the direction of flowing fluid across the stacked samples. Figure 4a presents the changes in pressure gradient/drop for the moving fluid across the stacked samples for different porous sample thickness with inlet and exit effect. This behaviour can be likened to the pattern of fluid flow characterised by sudden enlargement and contraction in open conduits. The flow of fluid downstream the vicinity of the larger pores to smaller ones (contraction) causes an increase in pressure

loss, resulting in a region of separated flow which occurs at the contraction point. Figure 4(Y2) shows that the flow is severely disrupted as a result of the contour changes in the downstream flowing fluid within the pore walls. Conversely, the flow of fluid from smaller pores to larger ones can be described as sudden enlargement of the pore volume available for the flowing fluid. Observably, this results in the creation of an unstable pattern of flow eddies (reverse current largely dictated by high fluid velocity in the turbulent regime) at the expansion zone, and hence, a significant decrease in pressure drop within the porous material. The extent to which the pressure drop across the stacked samples lies within the two individually computed sample values was also determined by their porous layer thickness. That is, for a long enough Inc 450 µm sample (low pore sizes), twice that of the Inc 1200 µm (Y1 & Y2), developed pressure drop is evidently (Fig. 4a) closer to the unit pressure drop of the original Inc 450 µm and this reduces significantly with reduced thickness taken from the sample (Z1 & Z2). This is likely due to the increasing pore non-uniformity of the longer Inc 450 µm in the
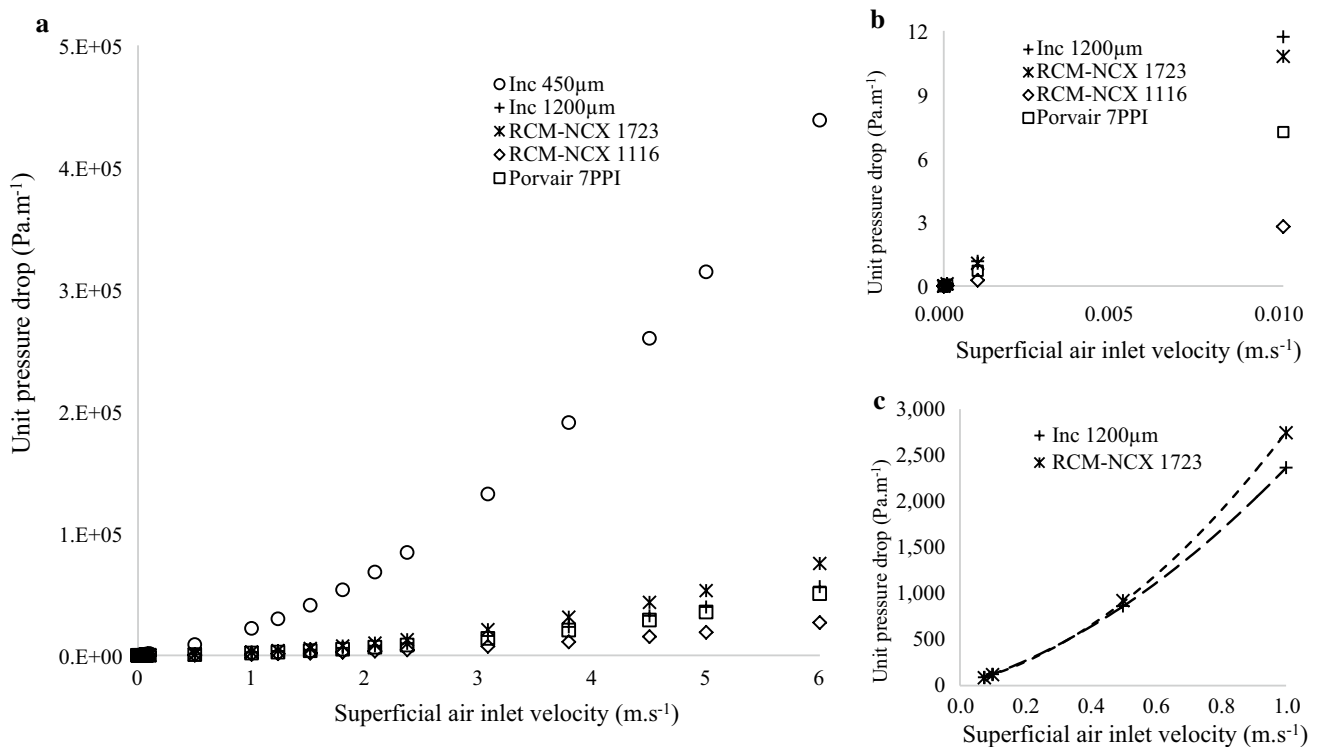
Fig. 3 Plots of the unit pressure drop (Pa m^{-1}) against superficial fluid velocity for **a** all the high-density porous metals at Darcy–turbulent **b** Darcy regime flow of fluid for samples excluding Inc 450 μm and **c** pore-structure effects on the pressure drop across Inc 1200 μm and RCM-NCX 1723 samples

Table 1 A tabular representation of the pore-structure and flow information of the high-density porous metallic structures

Samples		Dp (mm)	Dw (mm)	ε (%)	L_G (mm)	σ_{FB} (mm^{-1})	σ_{FF} (mm^{-1})	Darcy k_0/10^{-09} (m^2)	Forchheimer–turbulent k_0/10^{-09} (m^2)	C (m^{-1})	C_F
Inconel 450 μm	A	0.450	0.239	0.835	0.059	8.626	43.817	1.25	1.60	8541.55	0.342
Inconel 1200 μm	B	1.230	0.489	0.906	0.176	3.216	31.095	15.56	22.64	1183.95	0.178
RCM-NCX 1723	D	1.855	0.691	0.809	0.254	3.010	12.800	16.89	22.69	1628.87	0.245
RCM-NCX 1116	C	2.454	1.286	0.898	0.341	1.519	13.281	65.36	92.62	594.66	0.181
Porvair 7PPI	E	1.466	0.858	0.897	0.405	2.254	19.602	25.14	42.04	1105.67	0.227

Dp, pore sizes; Dw, pore connectivity; ε, pore volume fraction; L_G, ligament thickness; σ_{FB}, ratio of the structure surface area to bulk volume; σ_{FF}, ratio of the structure surface area to structure volume; k_0, permeability of the porous materials; C, Form drag coefficient; C_F, Forchheimer coefficient

stacked samples resulting in increasing tortuous path [17], hence, a higher pressure drop for the flowing fluid.

A measure of the accuracy of the modelling approach was achieved by comparing the CFD modelled values of unit pressure drop, permeability and Form drag coefficient for the Inc 450 μm foam sample with experimentally measured data in [1, 18] of fluid flow across a 20 mm thick sample of the "real" structure. For an experimentally measured effective pore volume fraction (ε) of 0.839 and superficial air inlet velocity ranging between 0.5 and 4.5 m s^{-1}, the agreements between the measured [1, 18] and CFD modelled values of

unit pressure drop developed across the porous structure were good and within reasonable scatter as shown in Fig. 5. Additionally, the measured values of permeability and Form drag coefficient for the 20 mm thick Inc 450 μm sample are $1.69 \pm 0.03 \times 10^{-09}$ m^2 and 8566.4 ± 150 m^{-1} respectively. The CFD computed values of the permeability and Form drag coefficient for this range of superficial fluid velocities are 1.60×10^{-09} m^2 and 8530.8 m^{-1} respectively, showing excellent agreement between measured and simulated values. It is of interest to note that a similar pore-level CFD approach used to quantify the pressure drop of low-density
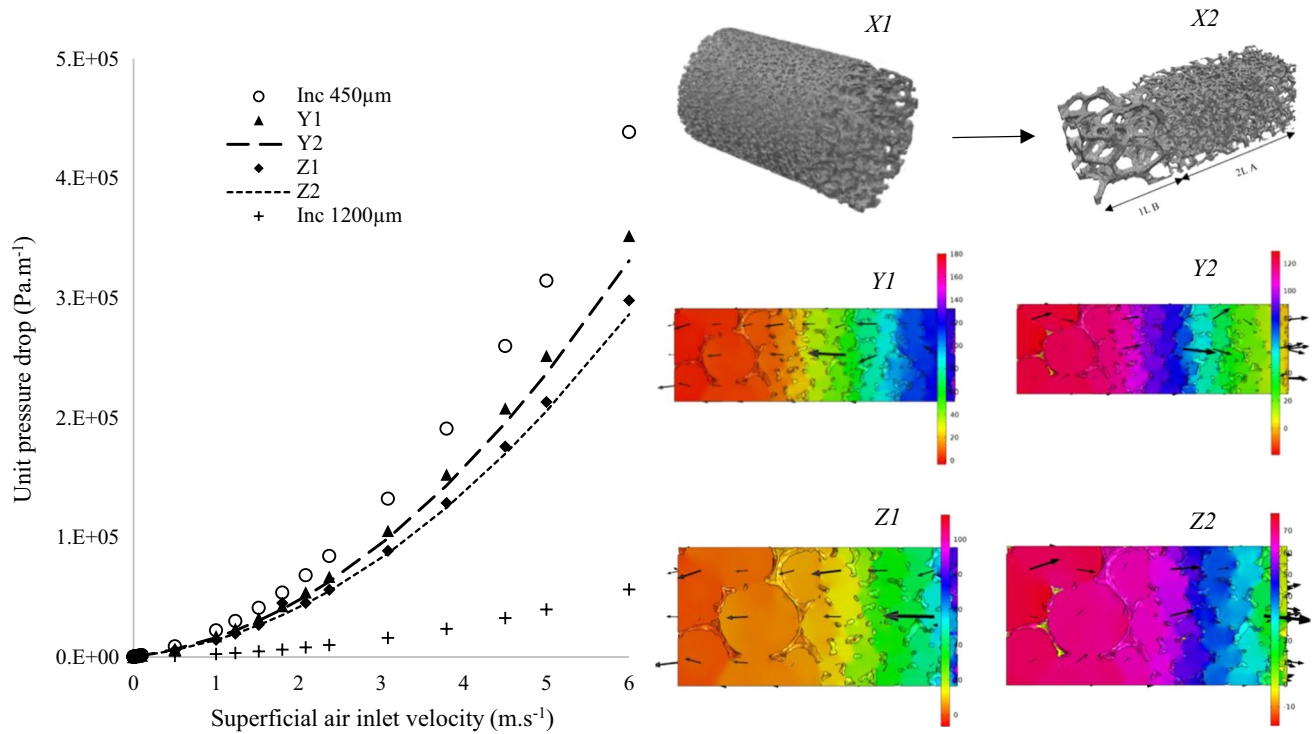
Fig. 4 Left of the 3D processed images and pressure profile plots is the unit pressure drop (Pa) developed across stacked samples of Inc 450 μm and Inc 1200 μm against superficial fluid inlet velocity (m s^{-1})

Fig. 5 Plots of measured [1, 18] and CFD modelled [Current] unit pressure drop against superficial air inlet velocity for Inconel 450 μm porous metallic structure

$$y = 10277x^2 + 11398x$$
$$R^2 = 1$$

$$y = 10320x^2 + 10803x$$
$$R^2 = 0.9999$$
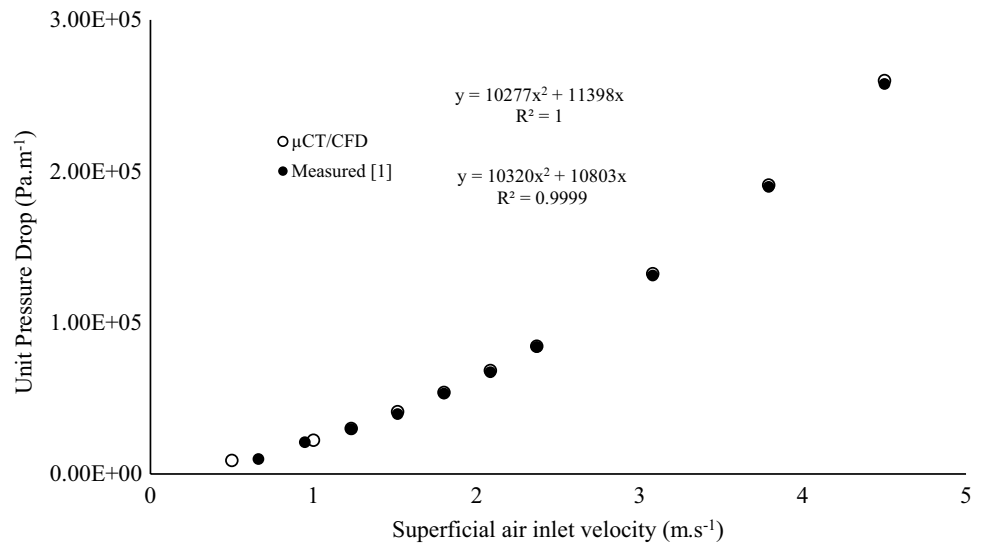
"bottleneck" dominated porous aluminium structures made by a replication-casting process by the leading author of this paper (published in [9]) shows reasonable correlations when compared with the experimental measurements.

In conclusion, investigation of the pressure drop of flowing fluid across high-density porous metallic structures has been presented utilising high-resolution tomography data for fluid superficial inlet velocity ranges between 0 and 6 m s^{-1}. Understanding the potential of mass transfer across these structures was done by using samples of different pore morphology varying in degree of pore size, pore connectivity and interstices. The combined modelling approach of 3D advanced imaging techniques and computational fluid dynamic modelling and simulation enabled an in-depth understanding of the changes in pressure

gradient/drop resulting from the sudden change in pore volume and sizes and entrance and exit effects.

References

1. A.J. Otaru, H.P. Morvan, A.R. Kennedy, AIChE J. **65**, 1355–1364 (2019)
2. A.J. Otaru, A.R. Kennedy, ASME Fluids Eng. (2019). https://doi.org/10.1115/1.4042957
3. P.R. Gunjal, V.V. Ranade, R.V. Chaudhari, AIChE J. **51**, 365–378 (2005)
4. N. Dukhan, DESTECH Publication, Inc. Technology & Engineering (2013) p. 52–55
5. A. Dellaorre, G. Montenegro, G.R. Tabor, M.L. Wears, Int. J. Heat Fluid Flow **50**, 72–82 (2014)
6. F. Lucci, A. Della Torre, G. Montenegro, R. Kaufmann, P.D. Eggenschwiler, Int. J. Heat Fluid Flow **108**, 341–350 (2017)
7. H. Oun, A.R. Kennedy, J. Porous Mater. **21**, 1133–1141 (2014)
8. A.J. Otaru, A.R. Kennedy, Scripta Mater. **124**(2016), 30–33 (2016)
9. A.J. Otaru, H.P. Morvan, A.R. Kennedy, Acta Mater. **149**, 265–275 (2018)
10. A.J. Otaru, H.P. Morvan, A.R. Kennedy, Scripta Materialia **150**, 152–155 (2018)
11. J.F. Despois, A. Mortensen, Acta Materialia **53**, 1381–1388 (2005)
12. A. Kouidri, B. Madani, Mech. Mater. **99**, 79–87 (2016)
13. A.J. Otaru, Met. Mater. Int. (2019). https://doi.org/10.1007/s12540-019-00345-9
14. J.L. Lage, P.S. Krueger, A. Narasimham, Phys. Fluids **17**, 088101 (2005)
15. S. Whitaker, Transp. Porous Media **1**, 3–25 (1986)
16. A. Dybbs, R.V. Edwards, J. Bear M.Y. Nato ASI series E (1984)
17. Y. Champoux, M.R. Stinson, J. Acoust. Soc. Am. **92–2**, 1120–1131 (1992)
18. A.J. Otaru, Unpublished Ph.D. Thesis at the University of Nottingham, United Kingdom (2018)